Analysis of Multipactor Effects by a Particle-in-Cell Algorithm Integrated With Secondary Electron Emission Model on Irregular Grids

Dong-Yeop Na, *Student Member, IEEE*, and Fernando L. Teixeira, *Fellow, IEEE*

***Abstract*— We combine a novel finite-element-based electromagnetic particle-in-cell (EM-PIC) algorithm for the solution of Maxwell–Vlasov equations on irregular (unstructured) grids together with the Furman–Pivi probabilistic model governing the secondary electron emission process. The algorithm can be used for the analysis of resonant electron discharging phenomena (multipactor effects) in high-power radio frequency devices. In contrast to previous algorithms, the present EM-PIC algorithm yields a self-consistent time update of fields and particles on irregular grids with energy and charge conservation obtained from first principles. The use of unstructured grids enables local mesh refinement and simulation of complex geometries with minimal geometric defeaturing. We apply the algorithm to model multipactor effects on waveguides with flat or corrugated walls. We contrast the evolution of the electron population in various cases and investigate the respective saturation processes arising from self-field counterbalancing effects.**

***Index Terms*— Maxwell–Vlasov equations, multipactor, particle-in-cell (PIC), secondary electron emission (SEE).**

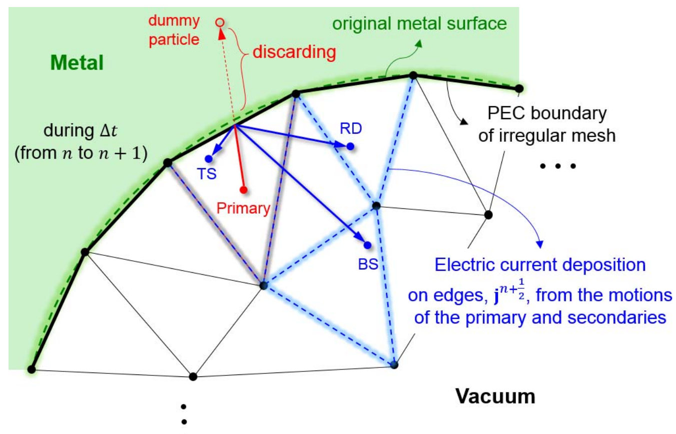

Fig. 1. Schematic illustration of a typical SEE process in an irregular-grid-based EM-PIC simulation. Note that electric current densities by the primary or secondaries are deposited on red- or blue-highlighted edges, respectively.

I. INTRODUCTION

RESONANT electron discharges from metallic or dielectric surfaces, also known as *multipactor* effects, are often observed in high-power radio frequency (RF) devices such as accelerators, vacuum tubes, and satellite payloads [1]. This effect generally degrades and limits device performance [2]–[5]. On the other hand, discharge effects can be harnessed by various technologies including electron guns, plasma displays, and for energy dissipation to protect highly sensitive receivers [6]. As a bridge between the theoretical and experimental analysis, computer simulations have been employed in recent years to analyze multipactor effects [7]–[10] via electromagnetic particle-in-cell (EM-PIC) algorithms [11]–[14], which basically solve Maxwell–Vlasov equations for tracking the nonlinear evolution of coarse-grained distribution of charged particles (tenuous plasma) and its interaction with the RF field.

In this paper, we numerically investigate multipactor effects using a novel EM-PIC algorithm based on the finite-element time-domain method implemented on unstructured (irregular) grids [15], [16]. The use of unstructured grids enables local mesh refinement and simulation of complex geometries with minimal geometric defeaturing, see Fig. 6. The present algorithm attains energy and charge conservation [16], a feature that has eluded previous EM-PIC algorithm implementations on irregular grids. In addition, the present algorithm implements the Furman–Pivi probabilistic model [17], based on a broad phenomenological fit to experiment data, to obtain accurate simulations of secondary electron emission (SEE) process (rather than a conventional monoenergetic one). We illustrate the proposed algorithm by examining multipactor effects taking place on waveguides with flat or corrugated (triangularly grooved) walls. We contrast the evolution of the electron population in various cases and investigate the respective saturation process arising from self-field counterbalance effects.

II. IRREGULAR-GRID EM-PIC ALGORITHM INTEGRATED WITH FURMAN–PIVI MODEL

EM-PIC algorithms are an effective means of modeling Maxwell–Vlasov equations describing the interaction of

Manuscript received October 5, 2018; revised December 12, 2018; accepted January 7, 2019. Date of publication January 25, 2019; date of current version February 11, 2019. This work was supported in part by the National Science Foundation under Grant ECCS-1305838, in part by Defense Threat Reduction Agency under Grant HDTRA1-18-1-0050, in part by the Ohio Supercomputer Center under Grant PAS-0061 and Grant PAS-0110, and in part by The Ohio State University Presidential Fellowship Program. The review of this paper was arranged by Senior Editor D. A. Shiffler. *(Corresponding author: Fernando L. Teixeira.)*

The authors are with the Department of Electrical and Computer Engineering, The Ohio State University, Columbus, OH 43212 USA (e-mail: na.94@osu.edu; teixeira.5@osu.edu).

Color versions of one or more of the figures in this paper are available online at http://ieeexplore.ieee.org.

Digital Object Identifier 10.1109/TPS.2019.2892323

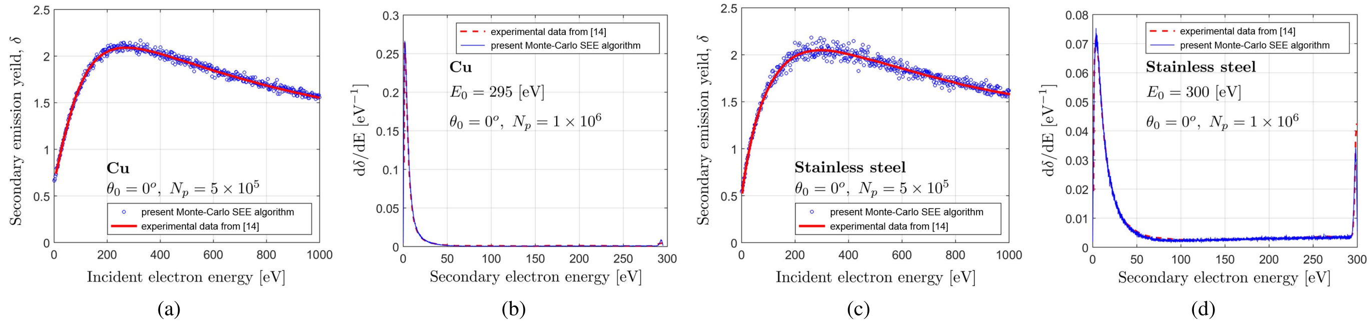

Fig. 2. Comparison of simulation and experimental results for SEE on copper [(a) and (b)] and stainless steel [(c) and (d)] surfaces. (a) and (c) SEY δ versus the primary incident energy. (b) and (d) Emitted-energy spectrum $d\delta/dE$.

time-varying electromagnetic fields and a large collisionless system of charged particles. Due to computational constraints, PIC algorithms are based on a coarse-graining of the phase space where the collection of charged particles is replaced by a smaller set of superparticles. The temporal dynamics of each superparticles is simulated by performing four serial operations at each time step during a marching-on-time simulation: 1) field update; 2) gather; 3) particle pusher; and 4) scatter. The details on the present Maxwell–Vlasov EM-PIC solver can be found in [15], [16], [18], and [19]. In addition, the scatter strategy for attaining charge conservation from first principles on irregular grids is summarized in Appendix A. We next discuss the integration of the probabilistic Furman–Pivi SEE model into the algorithm.

In this model [17], three types of (macroscopic) mechanisms producing secondary electrons are incorporated: 1) backscattered (BS) or almost elastic; 2) rediffused (RD) or partially elastic; and 3) true secondary (TS) or inelastic. A typical scenario for the SEE process during one-time step Δt (i.e., from time-step n to $n+1$) in the EM-PIC algorithm is illustrated in Fig. 1. When the primary electron (red solid line) trajectory intersects a metallic surface, the SEE algorithm launches secondaries (BS, RD, or TS, indicated by blue solid lines) via a stochastic process governed by the primary electron kinetic energy and incidence angle. Once all trajectories of the secondary electrons are obtained, the scatter step in the EM-PIC algorithm converts the electron trajectories into equivalent electric currents along edges of the irregular grid. In this process, the trajectory of the primary inside the metal (red dashed line) is discarded and the primary becomes dummy. As noted, the use of irregular grids enables a more accurate description of complex geometries, including curved and textured surface treatments employed to suppress the multipactor effects [20] or found in electron gun technologies. In the present EM-PIC algorithm, implementation of electron emission process from curved boundaries is more natural than in regular-grid-based EM-PIC algorithms. This is because the latter necessitates the use of *ad hoc* cut-cell methods or conformal finite-difference approaches [21]. For the purpose of implementing the *field* boundary conditions, the metallic surfaces are assumed as perfect electric conductors (PECs) at RF frequencies. A summary description and a pseudocode implementing the SEE process are provided in Appendix B.

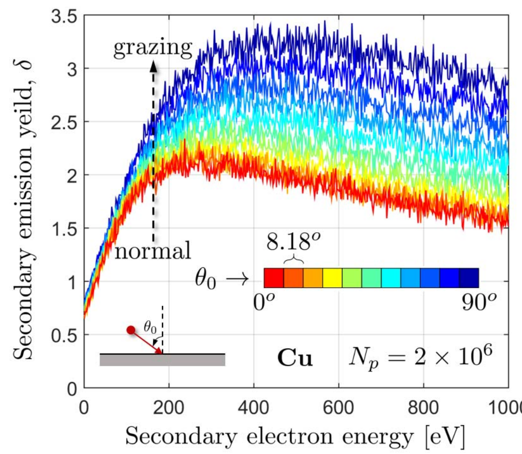

Fig. 3. Angular dependence of δ on a copper surface.

III. Numerical Results and Discussion

A. Verification of SEE Model in EM-PIC Simulations

In order to validate the probabilistic SEE process for embedding in present EM-PIC algorithm, we carried out impact simulations on copper and stainless steel surfaces without external fields. We obtained statistical averages of two important parameters: the secondary electron yield (SEY) δ and the emitted-energy spectrum $d\delta/dE$. We compare the simulation results against experimental data from [22].

Fig. 2(a) and (c) plots δ versus the incident electron energy (eV) for normal incidence when the superparticle number N_p is set equal to 5×10^5, for copper and stainless steel surfaces, respectively. Fig. 2(b) and (d) shows $d\delta/dE$ versus the secondary electron energy assuming primary impact energy $E_0 = 295$ (eV) and $E_0 = 300$ (eV), respectively, and normal incidence. The superparticle number N_p in these simulations is 1×10^6. Overall, there is a very good agreement between the present simulation results and the experimental data. We also tested the angular dependence of the SEE process for various primary incident angles. This is shown in Fig. 3, where it can be seen that grazing incidence generates more secondaries than the normal incidence, as expected. Note that the present algorithm assumes the same angular distribution function (cosine-like) as introduced in [17].

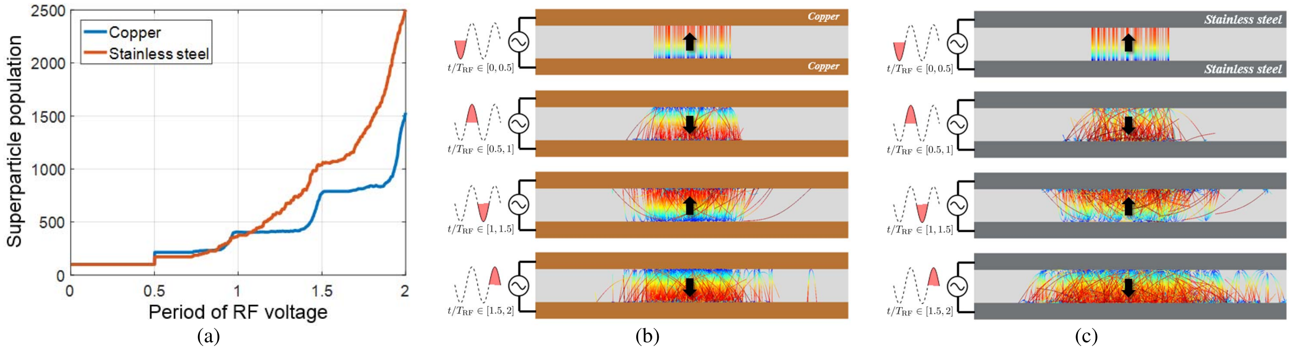

Fig. 4. PIC results for probabilistic SEE model. (a) Superparticle population versus time (RF voltage periods). (b) and (c) Snapshots of particle's trajectories for copper and stainless steel cases, respectively. These trajectory snapshots are taken during four successive half-periods of the RF signal, i.e., $t/T_{\mathrm{RF}} \in (0, 0.5)$, $t/T_{\mathrm{RF}} \in (0.5, 1)$, $t/T_{\mathrm{RF}} \in (1, 1.5)$, and $t/T_{\mathrm{RF}} \in (1.5, 2)$, where $T_{\mathrm{RF}} = 1/f_{\mathrm{RF}} = 0.96$ (ns).

B. Multipactor on Copper Versus Stainless Steel Surfaces

Consider parallel metallic plates separated by a 2-mm gap. An external RF voltage is applied to the plates as shown in Fig. 4(b) and (c). We assume a RF voltage with amplitude $V_{\mathrm{RF}}^{a} = 300$ V and frequency $f_{\mathrm{RF}} = 1.044$ GHz. These parameters are chosen to meet the multipactor resonant condition, see (1). We initially place 100 seed superparticles uniformly distributed along a line parallel to and near the lower plate. Each superparticle (both as initial seeds and future secondaries) in the simulation represents about 2.5×10^{8} actual electrons. Here, and in what follows, the metallic surfaces are assumed as PEC surfaces for the purpose of implementing the field boundary conditions in the RF frequency regime. The left and right ends of the grid are terminated by a perfectly matched layer [23]. Copper and stainless steel have different δ profiles, cf. Fig. 2(a) and (c) in [17]. Except for primary impacts with very low incident energy, electron avalanches can occur since δ is overall larger than unity. It is worth noting that in the copper plates most of the secondaries tend to be TS. On the other hand, both BS and TS electrons are prevalent in the stainless steel plates. Fig. 4 shows some EM-PIC simulation results that capture the distinct features in copper and stainless steel. In Fig. 4(a), we compare the temporal growth of superparticle population between the plates over the first two periods of the RF voltage. A nearly stepwise increase of the population can be observed in the copper plate whenever primary electrons hit the walls since the most of SEE is produced by TS emission and they are regularly accelerated along the retarding RF voltage. On the other hand, in the stainless steel plate, the net superparticle population increases rather more gradually due to the balance between almost elastic and inelastic secondary emissions. This implies that roughly half of electrons, which are of TS and BS, feel an accelerating force (in-phase) from the RF field while the remaining electrons are not in phase; however, this is enough for them to hit the wall so that net electron avalanches also occur. This is evidenced in Fig. 5, which illustrates the particles' trajectory in the phase space for successive half cycles of the RF signal. In these plots, the particle trajectories are colored with respect to their speed (faster by red lines, slower by blue lines). The axes represent the spatial coordinates, $x/10$ and y m, versus normalized speed of the particles $|\mathbf{v}_p|/20c$ for each half of the RF voltage period, as indicated. It can be observed that, for the second half-period, the stainless steel surface creates more energetic electrons at the moment of the emission than the copper surface. As a result, they produce more primary impacts that are out of phase with the RF field (in addition to the regularly accelerated ones). This causes the total electron population to increase gradually in the stainless steel case rather than the stepwise sense as in the copper case, see also Fig. 4(a).

TABLE I

MULTIPACTOR SIMULATION PARAMETERS FOR THE PARALLEL WAVEGUIDE IN FIG. 6(a)

D_{pp} [mm]	f_{RF} [GHz]	V_{RF}^{a} [V]	L_{pp} [mm]	L_{mp} [mm]
2	2	1,143	150	30

C. Surface Treatment Effects

Consider a waveguide with copper plates separated by a gap size D_{pp} m and longitudinal length L_{pp}, as depicted in Fig. 6(a). In this case, a transverse electromagnetic wave is injected from the input (left) port by exciting a line current source between the plates. The output voltage is measured at the right-end port. We denote f_{RF} and V_{RF} as the frequency and RF voltage amplitude of the input signal. Initially, we place 1000 superparticle seeds uniformly distributed near the lower plate and launch them with zero velocities [the electron cloud region in Fig. 6(a)]. Each superparticle represents 2×10^{7} actual electrons. In order to prevent stray electrons spreading laterally, it is assumed that only the central section of length L_{mp} [blue-glowed-solid lines in Fig. 6(a)] are constituted by copper yielding the secondaries. The other surfaces are assumed as collectors that absorb electrons. The multipactor resonant condition is given by

$$f_{\mathrm{RF}} = \frac{1}{2\sqrt{\pi}\, D_{\mathrm{pp}}} \sqrt{V_{\mathrm{RF}}^{a} \frac{q_e}{m_e}} \quad (\mathrm{Hz}) \tag{1}$$

where q_e and m_e are the charge and mass for an electron. All parameters are chosen to meet the resonant condition

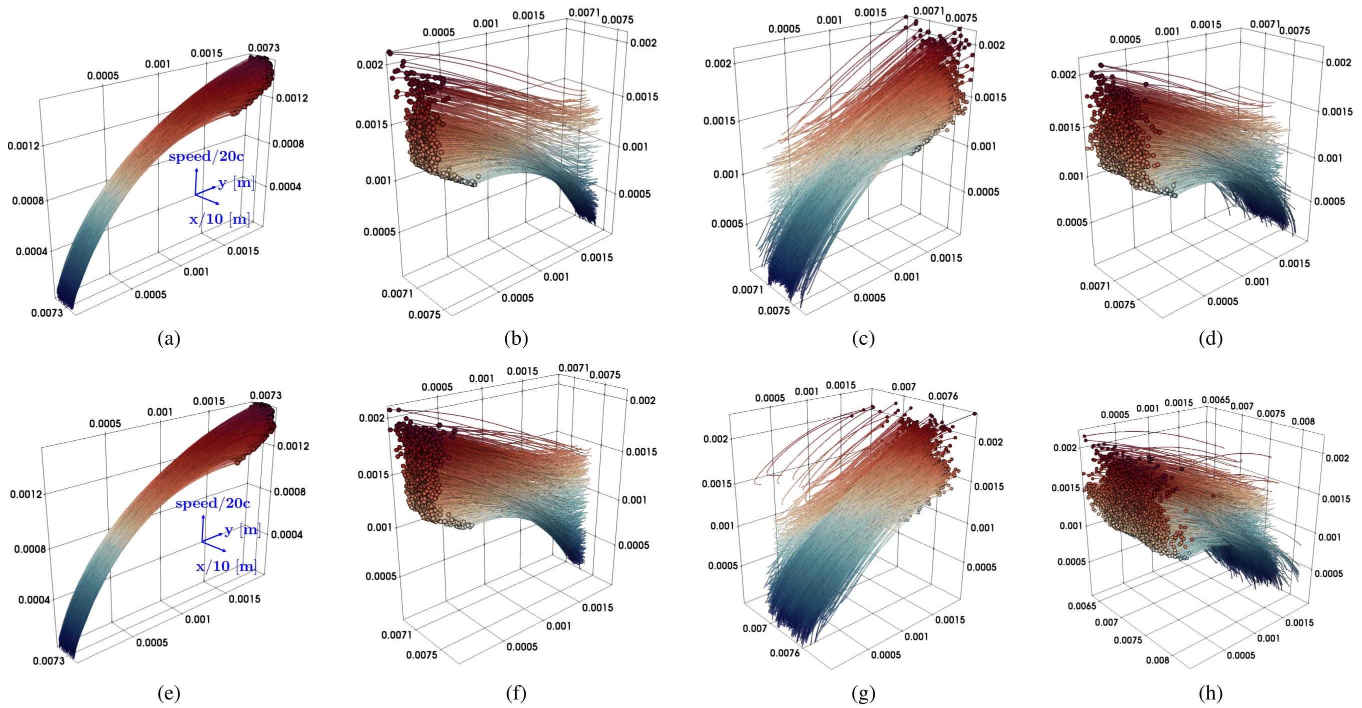

Fig. 5. Particle trajectory snapshots on the phase space. The coordinate axes represent $x/10$ [m], y [m], and the normalized speed of the particles ($|\mathbf{v}_p|/20c$). Each plot corresponds to a half-period of the RF signal, as in Fig. 4. (a) $t/T_{\mathrm{RF}} \in (0, 0.5)$, copper. (b) $t/T_{\mathrm{RF}} \in (0.5, 1)$, copper. (c) $t/T_{\mathrm{RF}} \in (1, 1.5)$, copper. (d) $t/T_{\mathrm{RF}} \in (1.5, 2)$, copper. (e) $t/T_{\mathrm{RF}} \in (0, 0.5)$, stainless steel. (f) $t/T_{\mathrm{RF}} \in (0.5, 1)$, stainless steel. (g) $t/T_{\mathrm{RF}} \in (1, 1.5)$, stainless steel. (h) $t/T_{\mathrm{RF}} \in (1.5, 2)$, stainless steel.

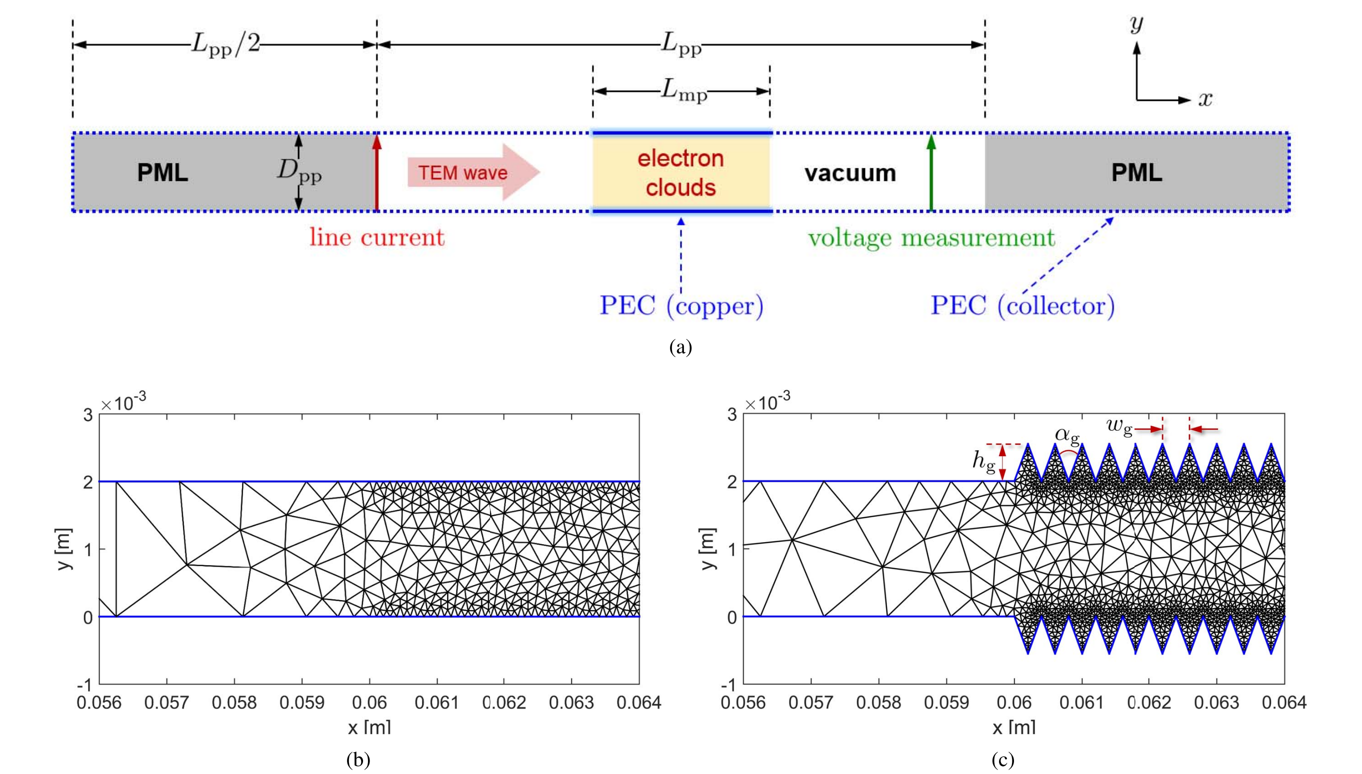

Fig. 6. Multipactor in parallel plate waveguides. (a) Schematics of the problem geometry. (b) Flat surface waveguide meshing. (c) Triangular-grooved waveguide meshing.

and represented in Table I. We consider two types of surfaces: flat and triangularly grooved surfaces, as illustrated in Fig. 6(b) and (c), respectively. The width, depth, angle, and number of grooves are denoted as w_g, h_g, α_g, and N_g, respectively, and their values are given in Table II. Note that a triangularly grooved surface might reduce δ depending on

TABLE II
TRIANGULARLY GROOVED SURFACE PARAMETERS

w_g [mm]	h_g [mm]	α_g [deg.]	N_g
0.2	0.5495	40	150

TABLE III
MESH PARAMETERS

	N_0	N_1	N_2	$\Delta t_{\max}$ [fs]
flat surface	2,913	7,823	4,911	135
grooved surface	11,394	31,476	20,083	75

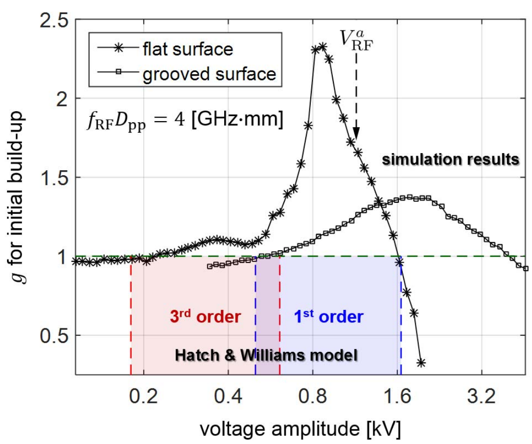

Fig. 7. RF voltage amplitude susceptibility at $f_{\rm RF}D_{\rm pp} = 4$ (GHz · mm) for flat and grooved copper surfaces.

α_g, as discussed in [20]. The domain is discretized using an unstructured mesh. Table III lists some of the mesh parameters: N_0, N_1, and N_2 are the number of nodes, edges, and faces, respectively. In addition, $\Delta t_{\max}$ denotes the maximum time-step interval for stable simulations according to the Courant–Friedrichs–Lewy criterion. Both simulations adopt $\Delta t = 50$ (fs). In order to accurately capture the behaviors of fields around the grooved surface, we apply a local mesh refinement near the tips, as shown in Fig. 6(c).

D. Multipactor Susceptibility to RF Voltage Amplitude

In order to examine the multipactor susceptibility to the RF voltage amplitude, we observed the electron population multiplication during the first five RF voltage periods (initial build-up) and for different RF voltage amplitudes. Reference [24] noted that the rate of change in the number of stray electrons over time to provide a measure of multipactor susceptibility. Here, we introduce a gain factor g as

$$g = \left(N^{n_f}_{p,\text{eff}}/N^{n_s}_{p,\text{eff}}\right)^{1/[2f_{\rm RF}(n_f-n_s)\Delta t]} \tag{2}$$

where $N^n_{p,\text{eff}}$ denotes the number of superparticle flying between plates at the nth time-step, and the exponent represents the inverse of the total number of primary hits during the considered time interval $(n_f-n_s)\Delta t$. As noted, we choose $n_f = 2.5$ ns and $n_s = 0$ here. Multipactor occurs when $g > 1$ and becomes stronger for larger g, akin to the conventional δ.

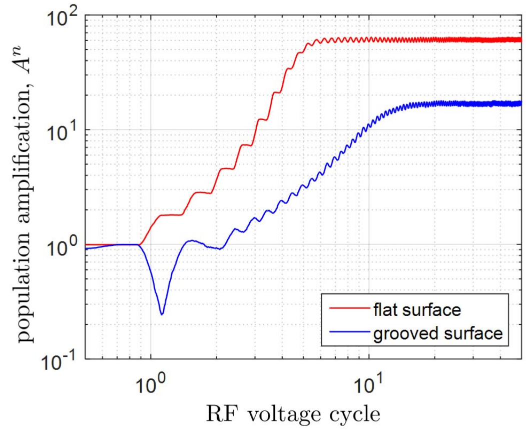

Fig. 8. RF voltage cycle versus population amplification, A^n for both surfaces at $V^a_{\rm RF} = 1143.16$ V.

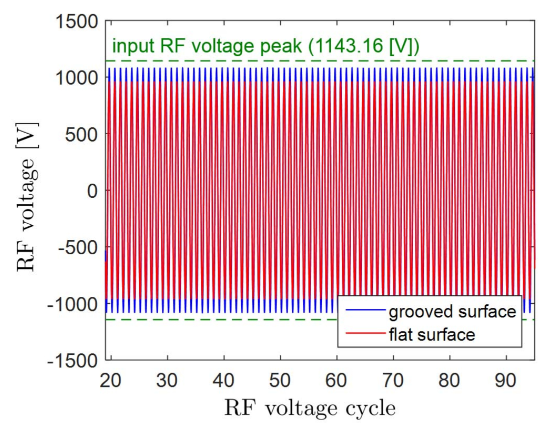

(a)

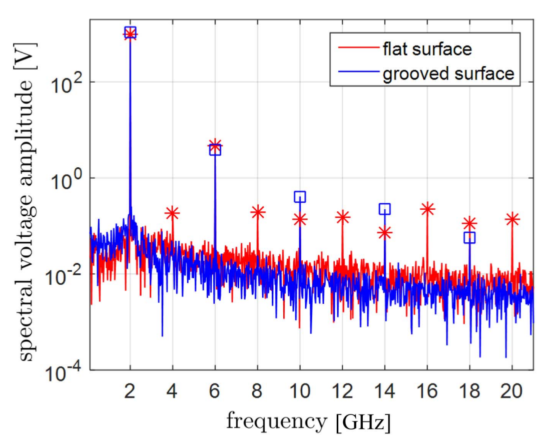

(b)

Fig. 9. Output signals for both surfaces. (a) Time-domain. (b) Frequency domain.

Fig. 7 illustrates RF voltage amplitude versus g for flat and grooved copper surfaces with $f_{\rm RF} \cdot D_{\rm pp} = 4$ GHz · mm. On the flat case, the simulations indicated that multipactor is triggered for RF voltage amplitudes $V_{\rm RF}$ in the range from about 200 to 1600 V. These simulation results are in a good agreement with range estimates from the Hatch–Williams model [22], represented by the red and blue shaded regions

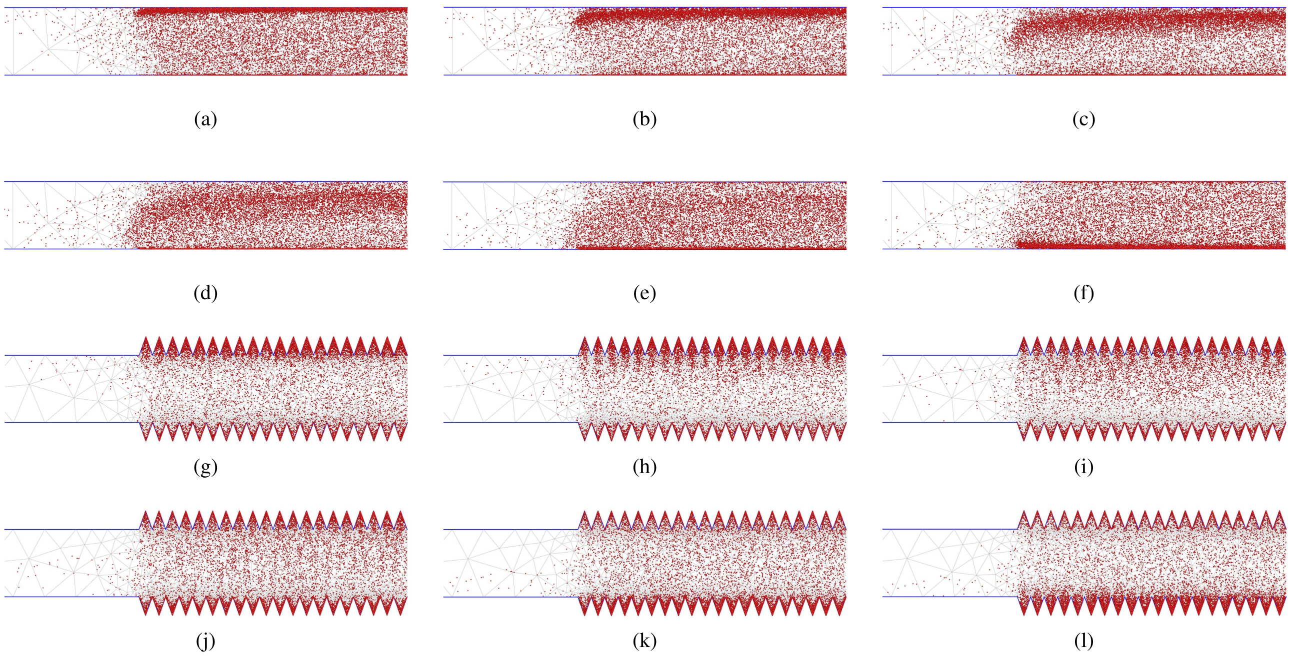

Fig. 10. Particle position snapshots taken over a half RF period during the saturation regime. The RF voltage period is 0.5 ns. (a)–(f) Flat surface. (g)–(l) Grooved surfaces.

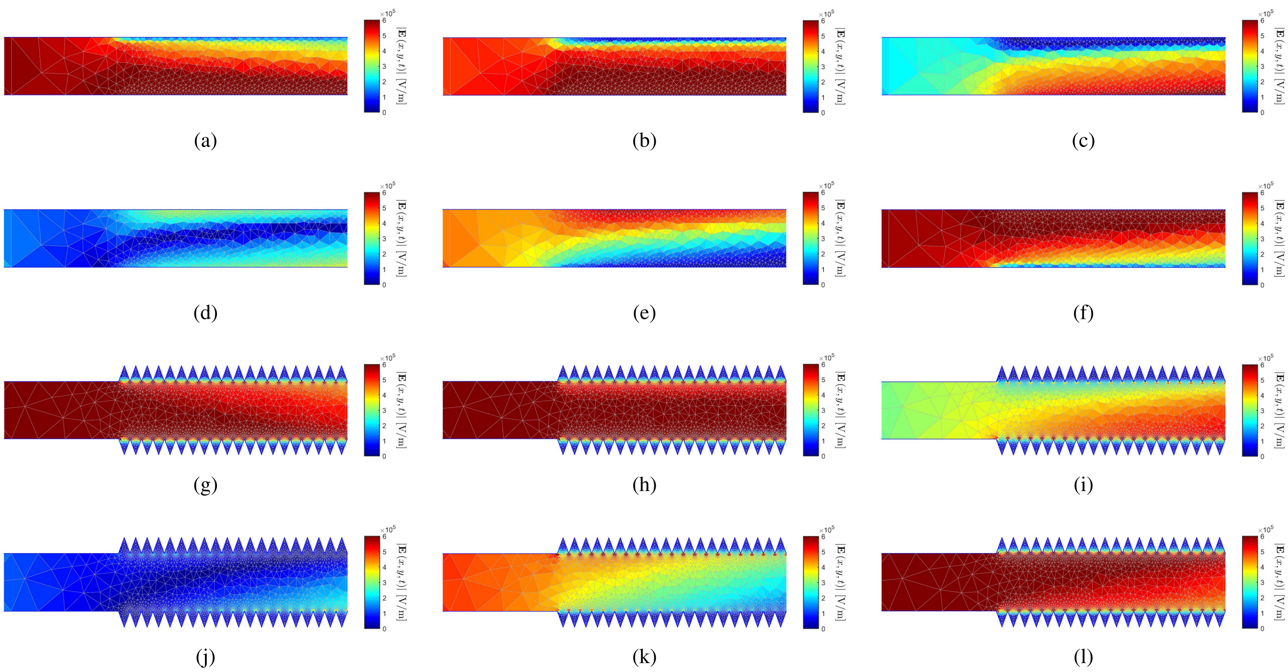

Fig. 11. External-field and self-field snapshots taken over a half period during the saturation regime. The RF voltage period is 0.5 ns. (a)–(f) Flat surface. (g)–(l) Grooved surfaces.

in Fig. 7. The peaks observed in the low (at about 0.35 kV) and high (at about 0.85 kV) voltage regimes result from third-order and first-order multipactor, respectively. In contrast to these results, the susceptibility band in the grooved case becomes wider and moves toward higher voltages as seen in Fig. 7. This can be explained by the fact that the effective gap size of the grooved waveguide is larger than the flat surfaced waveguide. For a fixed frequency, (1) predicts that the voltage amplitude should increase with an increase in the gap size.

E. Multipactor Saturation Effects

An exponential growth in the population of stray electrons can be observed during the initial build-up of multipactor. After many RF voltage cycles, the electron population saturates due to two main mechanisms: 1) acceleration-phase-mismatching and 2) the fact that secondary electrons are pulled back toward the surface by increasingly strong space-charge fields [25]. Some symptoms by multipactor saturation are output power loss and harmonic generation. In order to capture

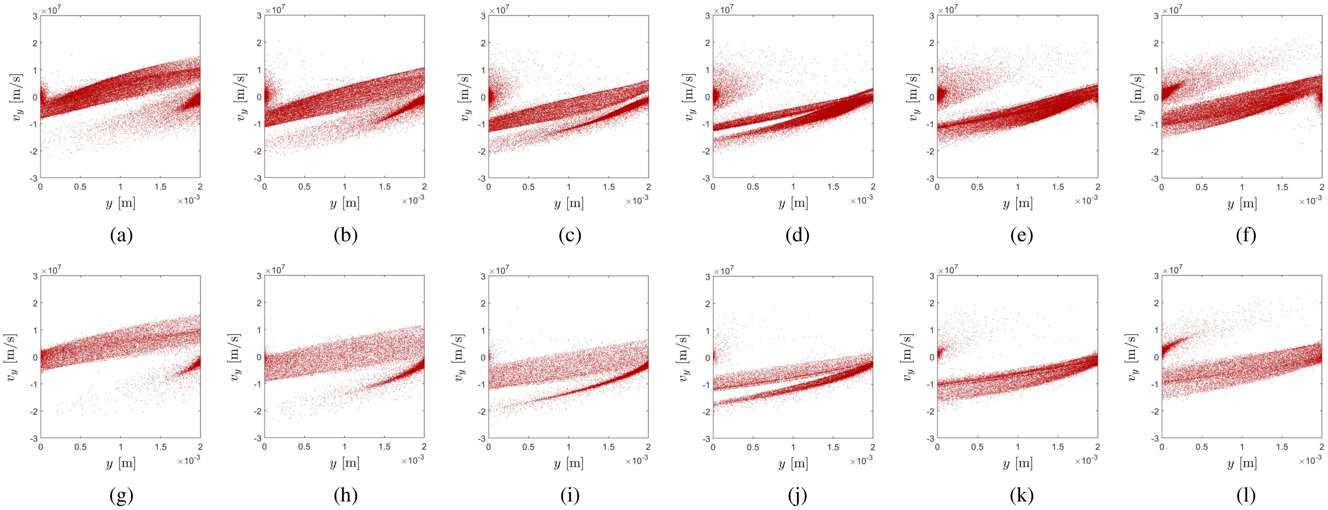

Fig. 12. Snapshots of v_x (m/s) versus y (m) taken over a half RF period during the saturation regime. The RF voltage period is 0.5 ns. (a)–(f) Flat surface. (g)–(l) Grooved surfaces.

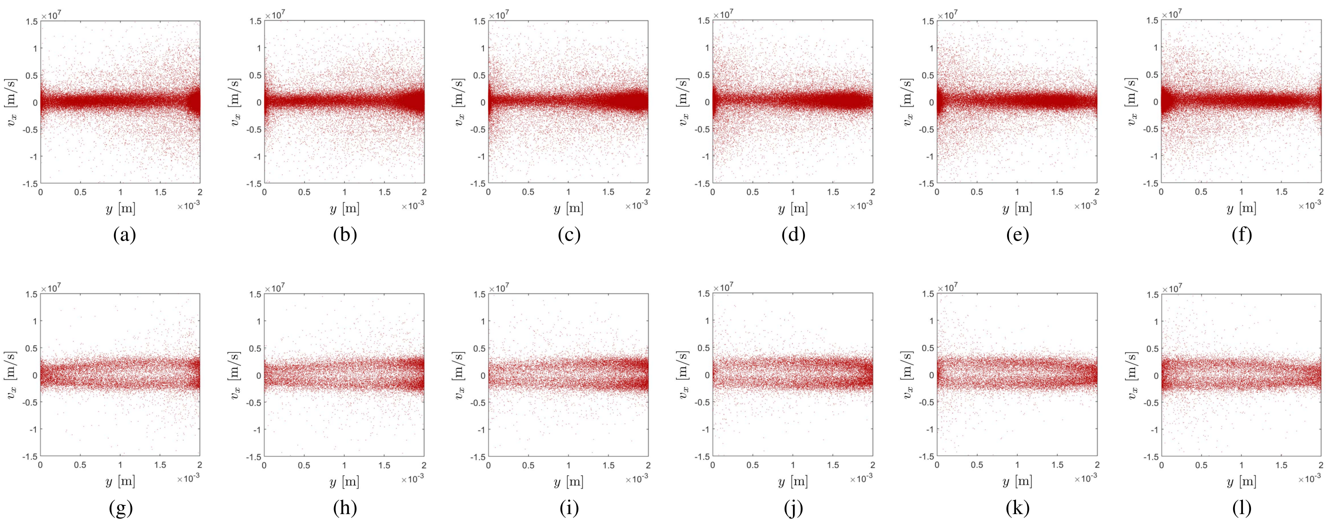

Fig. 13. Snapshots of v_x (m/s) versus y (m) taken over a half RF period during the saturation regime. The RF voltage period is 0.5 ns. (a)–(f) Flat surface. (g)–(l) Grooved surfaces.

the saturation phenomenon, based on the reference setting (i.e., with $V_{\mathrm{RF}}^{a} = 1143.16$ V), we ran EM-PIC simulations for 100 RF periods and for both types of surfaces. Fig. 8 shows the log-scale plot of the electron population amplification factor $A^n = N_p^n/N_p^0$, where N_p is the total number of superparticles flying between two metallic plates at time step n, versus the RF voltage cycle. The number density increases at an exponential rate up to an intermediate stage close to about six RF cycles, beyond which saturation is reached due to strong space-charge self-fields. During the intermediate stage, the amplitude of RF fields prevails over the space-charge self-field, and most secondaries successfully escape from the emission surface.

Fig. 9(a) shows the instantaneous RF voltage at the output port over time. As expected, the output voltage amplitudes in both cases are smaller than the input voltage amplitude (green dashed line, 1143.16 V). Their spectra are shown in Fig. 9(b) where it can be clearly seen that, in addition to the original 2 GHz signal, many frequency harmonics are generated in both cases.

Table IV compares the spectral amplitudes of each harmonic for both cases. It is seen that the flat case includes all harmonics (even and odd) but the grooved case exhibits only odd harmonics. According to [26], the output voltage signal should include only odd orders to the fundamental frequency $f_{0,N_{\mathrm{mp}}} = f_{\mathrm{RF}}/N_{\mathrm{mp}}$, which depends on the order of multipactor N_{mp} (here, $f_{\mathrm{RF}} = 2$ GHz). However, Fig. 9(b) shows that, in the flat surface case, both odd- and even-order harmonics are present. Similar results have been observed in [27]. The presence of even harmonics in the flat case might be due to the presence of stronger horizontal (lateral) currents due to drifting electrons with oblique SEE, which is not incorporated by the model considered in [26]. Further work is needed to test this hypothesis.

TABLE IV
SPECTRAL AMPLITUDE OF OUTPUT VOLTAGE SIGNALS FOR HIGH-ORDER HARMONICS

	flat surface	grooved surface
$f_{\text{RF}} = 2$ [GHz]	9.6620×10^{2}	1.0803×10^{3}
2^{nd} harmonic	1.8682×10^{-1}	-
3^{rd} harmonic	4.7680×10^{0}	3.8502×10^{0}
4^{th} harmonic	1.9876×10^{-1}	-
5^{th} harmonic	1.3681×10^{-1}	4.1402×10^{-1}
6^{th} harmonic	1.4994×10^{-1}	-
7^{th} harmonic	7.2536×10^{-2}	2.2400×10^{-1}
8^{th} harmonic	2.2514×10^{-1}	-
9^{th} harmonic	1.1574×10^{-1}	5.6164×10^{-2}
10^{th} harmonic	1.3934×10^{-1}	-
11^{th} harmonic	1.3888×10^{-1}	3.8213×10^{-2}

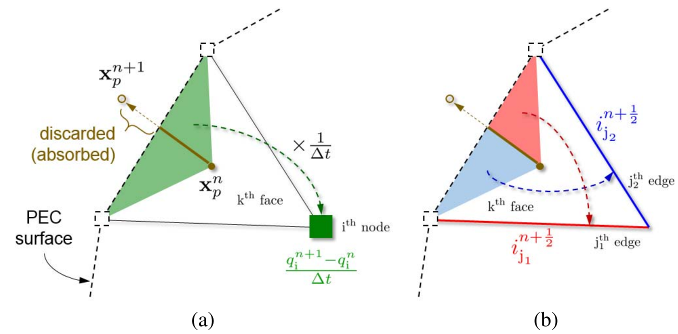

Fig. 14. Geometric illustration of exact charge conservation on irregular grids for a primary impact (also applicable for secondary electrons emitted on the opposite way) at PEC surfaces during Δt. (a) Charge variation rate at jth node. (b) Divergence of current on jth node, which is equal to the sum of ith and kth currents.

Figs. 10–13 show snapshots of particle and fields evolutions and phase plots (vertical and horizontal components of velocity), respectively, taken over a half RF period at the saturation regime for both surfaces. It is observed in Fig. 10 that many electrons inside the grooves experience multiple impacts. This effectively lowers down the average number of the secondaries launched to the surface. The breakdown of the focusing effect, which is one of the symptoms from multipactor saturation [25], [27], can be seen in Fig. 12 for both surfaces. Fig. 13 shows the influence of the external lateral electric field (horizontal component) present in the grooved geometry on the horizontal electron speed distribution.

IV. CONCLUSION

We have described the integration of a charge-conserving and energy-conserving finite-element-based EM-PIC algorithm implemented on unstructured (irregular) meshes with the Furman–Pivi probabilistic model describing SEE processes on metallic surfaces. The proposed SEE/EM-PIC algorithm enables mesh refinement and is better suited to model to complex geometries. The algorithm was validated by comparing simulation results with available prior data. The algorithm was applied to evaluate and compare multipactor effects on copper and stainless steel parallel plates. In addition, the algorithm was employed to compare multipactor on copper waveguides with flat or corrugated (triangularly grooved) walls. The multipactor saturation process was examined by quantifying the output power loss and harmonic generation arising from acceleration phase mismatching and self-field counterbalance effects.

APPENDIX A
CHARGE-CONSERVING SCATTER ON IRREGULAR GRIDS

Given a particle trajectory (motion) during one unit time interval Δt, the scatter step of a PIC algorithm assigns the consequent current onto the edges of the grid. This edge-based current subsequently enter as a source term in the Maxwell field solver (through the discrete Ampere's law). A major challenge for PIC algorithm has been how to develop charge conserving scatter schemes. Recently, a Whitney-form-based scatter [15], [28]–[30] based on exterior calculus of differential forms [29]–[34] was developed to attain charge conservation from first principles. Specifically, (the Hodge duals of) the current and charge densities are expanded by means of Whitney 1- and 0-forms, respectively [29], [30]. On an unstructured mesh, node-based charges and edge-based currents are obtained by integral evaluations of such forms at the charged particle's position and along its trajectory, respectively.

From Maxwell's equations, the tangential electric and magnetic field components at a PEC surface are zero. As such, the present field solver enforces zero tangential fields at the metallic surfaces. A charged particle next to a metallic surface will induce a surface charge distribution on the surface that can be obtained from image theory assuming a charged particle sufficiently close to a locally planar surface. As the charged particle approaches the surface from the grid domain, the fields due to the charged particle and its image will cancel each other. When the particle hits the surface, the associated field becomes zero and the charge is then absorbed (discarded) by the EM-PIC algorithm. On the grid, charge conservation is obtained by a proper balance between the variation of the node-based charges and the edge-based currents that touch a given node. This is illustrated in Fig. 14 when a single-charged particle inside the kth face (triangle) crossed the metallic (PEC) surfaces and leaves the problem domain (black dashed line), there is an associated nonzero grid charge at the ith node (green square) and associated currents at the j_1th (red) and j_2th (blue) edges. From a geometrical viewpoint, the grid charge variation rate on ith node, which from the Whitney 0-form expansion is associated with the green-colored area divided by Δt, is equal to the sum of the grid currents flowing in/out of the ith node, which is the sum of two grid currents at j_1th and j_2th edges. Form the Whitney 1-form expansion of the currents, the latter is equivalent to the sum of two areas colored in red and blue. A mathematical derivation of these results can be found in [15] and [16].

APPENDIX B
FURMAN–PIVI SEE MODEL IMPLEMENTATION

The basic steps implementing the probabilistic Furman–Pivi SEE model are summarized in the EM-PIC code, which are

Algorithm 1 Basic Steps for Implementation of SEE in the EM-PIC Algorithm

```
for p ∈ [1, 2, ..., N_{p,max}] do
    a ← Dummy_Effective_Checker(p);
    if a == 1 then
        v_p^{n+1/2} ← Particle_Acceleration(p);
        x_p^{n+1} ← Particle_Push(p);
        b ← Impact_Checker(p);
        if b == 1 then
            x_p^{imp} ← Impact_Position(p);
            d ← Impact_Energy(p);
            e ← Impact_Angle(p);
            j^{n+1/2} ← Scatter(x_p^n, x_p^{imp});
            Delete_Primary(p);
            N_{SEY} ← Compute_SEY(d,e);
            for q ∈ [1, 2, ..., N_{SEY}] do
                r ← Min_Dummy_Finder();
                Compute_Launch_Energy(r);
                Compute_Launch_Angle(r);
                x_r^{n+1} ← Particle_Push(r);
                j^{n+1/2} ← Scatter(x_p^{imp}, x_r^{n+1});
            end
        else
            j^{n+1/2} ← Scatter(x_p^n, x_p^{n+1});
        end
    end
end
```

summarized in Algorithm 1. Initially, a vacant 1-D workspace of size $N_{p,\max} \times 1$ is set for either dummy or effective macroparticles. At each time-step, a *for* loop is performed with respect to the index p that checks whether or not the pth particle is dummy by `Dummy_Effective_Checker`, yielding the integer a: 1 (effective) or 0 (dummy). If $a = 1$, `Particle_Acceleration` and `Particle_Push` accelerate and push the pth particle during one time-step, respectively, and yield its updated velocity $\mathbf{v}_p^{n+(1/2)}$ and position $\mathbf{x}_p^{n+1}$. Afterward, `Impact_Checker` tests the occurrence of the impact of pth particle on metal surfaces, producing the integer b: 1 (impact) or 0 (no impact). If $b = 0$, `scatter` uses $\mathbf{x}_p^n$ and $\mathbf{x}_p^{n+1}$ to compute grid electric currents, $\mathbf{j}^{n+(1/2)}$[1]. If $b = 1$, the SEE algorithm determines the impact position, energy, and angle via `Impact_Position`, `_Energy`, and `_Angle`, respectively. After the primary's trajectory between $\mathbf{x}_p^n$ to impact position $\mathbf{x}_p^{\text{imp}}$ is converted to an grid electric current, the primary particle is discarded (absorbed). In accordance with the impact information obtained earlier, the number of the secondaries N_{SEY} is computed by `Compute_SEY` based on the Furman–Pivi probabilistic SEE model. Another *for* loop is performed to compute the launching energy and angle for the secondaries. This information is saved in vacant bins found by `Min_Dummy_Finder`. Finally, the new secondaries are launched and their current transferred to the grid in the scatter step.

References

[1] J. R. M. Vaughan, "Multipactor," *IEEE Trans. Electron Devices*, vol. ED-35, no. 7, pp. 1172–1180, Jul. 1988.

[2] R. F. Parodi. (Dec. 2011). "Multipacting." [Online]. Available: https://arxiv.org/abs/1112.2176

[3] A. A. Hubble, V. H. Chaplin, K. A. Clements, R. Spektor, P. T. Partridge, and T. P. Graves, "Multipactor breakdown threshold reduction due to magnetic confinement in parallel fields," *IEEE Trans. Plasma Sci.*, vol. 45, no. 7, pp. 1726–1730, Jul. 2017.

[4] S. A. Rice and J. P. Verboncoeur, "Migration of multipactor trajectories via higher-order mode perturbation," *IEEE Trans. Plasma Sci.*, vol. 45, no. 7, pp. 1739–1745, Jul. 2017.

[5] A. Berenguer, A. Coves, F. Mesa, E. Bronchalo, and B. Gimeno, "Analysis of multipactor effect in a partially dielectric-loaded rectangular waveguide," *IEEE Trans. Plasma Sci.*, vol. 47, no. 1, pp. 259–265, Jan. 2019.

[6] R. Kishek, Y. Y. Lau, L. K. Ang, A. Valfells, and R. M. Gilgenbach, "Multipactor discharge on metals and dielectrics: Historical review and recent theories," *Phys. Plasmas*, vol. 5, no. 5, pp. 2120–2126, May 1998.

[7] J. Wang, L. Cai, X. Zhu, Y. Wang, and C. Xuan, "Numerical simulations of high power microwave dielectric interface breakdown involving outgassing," *Phys. Plasmas*, vol. 17, no. 6, p. 063503, 2010, doi: 10.1063/1.3432715.

[8] L. Cai, J. Wang, X. Zhu, Y. Wang, C. Xuan, and H. Xia, "Suppression of multipactor discharge on a dielectric surface by an external magnetic field," *Phys. Plasmas*, vol. 18, no. 7, p. 073504, 2011, doi: 10.1063/1.3602080.

[9] L. B. Cai, J. G. Wang, D. H. Zhang, T. J. Du, X. Q. Zhu, and Y. Wang, "Self-consistent simulation of the initiation of the flashover discharge on vacuum insulator surface," *Phys. Plasmas*, vol. 19, no. 7, p. 073516, 2012, doi: 10.1063/1.4737195.

[10] L. Cai, J. Wang, X. Zhu, Y. Wang, and D. Zhang, "Two-dimensional simulation research of secondary electron emission avalanche discharge on vacuum insulator surface," *Phys. Plasma*, vol. 22, no. 1, p. 013502, 2015, doi: 10.1063/1.4905640.

[11] J. W. You, H. G. Wang, J. F. Zhang, S. R. Tan, and T. J. Cui, "Accurate numerical method for multipactor analysis in microwave devices," *IEEE Trans. Electron Devices*, vol. 61, no. 5, pp. 1546–1552, Apr. 2014.

[12] J. W. You, H. G. Wang, J. F. Zhang, S. R. Tan, and T. J. Cui, "Accurate numerical analysis of nonlinearities caused by multipactor in microwave devices," *IEEE Microw. Wireless Compon. Lett*, vol. 24, no. 11, pp. 730–732, Nov. 2014.

[13] R. W. Hockney and J. W. Eastwood, *Computer Simulation Using Particles*. New York, NY, USA: CRC Press, 1988.

[14] J. G. Wang *et al.*, "UNIPIC code for simulations of high power microwave devices," *Phys. Plasmas*, vol. 16, no. 3, p. 033108, Mar. 2009.

[15] H. Moon, F. L. Teixeira, and Y. A. Omelchenko, "Exact charge-conserving scatter–gather algorithm for particle-in-cell simulations on unstructured grids: A geometric perspective," *Comput. Phys. Commun.*, vol. 194, pp. 43–53, Sep. 2015.

[16] D.-Y. Na, H. Moon, Y. A. Omelchenko, and F. L. Teixeira, "Local, explicit, and charge-conserving electromagnetic particle-in-cell algorithm on unstructured grids," *IEEE Trans. Plasma Sci.*, vol. 44, no. 8, pp. 1353–1362, Aug. 2016.

[17] M. A. Furman and M. T. F. Pivi, "Probabilistic model for the simulation of secondary electron emission," *Phys. Rev. ST, Accel. Beams*, vol. 5, p. 124404, Dec. 2002.

[18] D.-Y. Na, Y. A. Omelchenko, H. Moon, B.-H. V. Borges, and F. L. Teixeira, "Axisymmetric charge-conservative electromagnetic particle simulation algorithm on unstructured grids: Application to microwave vacuum electronic devices," *J. Comput. Phys.*, vol. 346, pp. 295–317, Oct. 2017.

[19] D.-Y. Na, H. Moon, Y. A. Omelchenko, and F. L. Teixeira, "Relativistic extension of a charge-conservative finite element solver for time-dependent Maxwell-Vlasov equations," *Phys. Plasmas*, vol. 25, no. 1, p. 013109, 2018.

[20] M. Pivi, F. K. King, R. E. Kirby, T. O. Raubenheimer, G. Stupakov, and F. Le Pimpec, "Sharp reduction of the secondary electron emission yield from grooved surfaces," *J. Appl. Phys.*, vol. 104, no. 10, p. 104904, 2008.

[21] C. S. Meierbachtol, A. D. Greenwood, J. P. Verboncoeur, and B. Shanker, "Conformal electromagnetic particle in cell: A review," *IEEE Trans. Plasma Sci.*, vol. 43, no. 11, pp. 3778–3793, Nov. 2015.

[22] A. J. Hatch and H. B. Williams, "Multipacting modes of high-frequency gaseous breakdown," *Phys. Rev.*, vol. 112, pp. 681–685, Nov. 1958.

[23] F. L. Teixeira and W. C. Chew, "Differential forms, metrics, and the reflectionless absorption of electromagnetic waves," *J. Electromagn. Waves Appl.*, vol. 13, no. 5, pp. 665–686, 1999.

[24] J. de Lara *et al.*, "Multipactor prediction for on-board spacecraft RF equipment with the MEST software tool," *IEEE Trans. Plasma Sci.*, vol. 34, no. 2, pp. 476–484, Apr. 2006.

[25] S. Riyopoulos, "Multipactor saturation due to space-charge-induced debunching," *Phys. Plasmas*, vol. 4, no. 5, pp. 1448–1462, 1997.

[26] E. Sorolla *et al.*, "An analytical model to evaluate the radiated power spectrum of a multipactor discharge in a parallel-plate region," *IEEE Trans. Electron Devices*, vol. 55, no. 8, pp. 2252–2258, Aug. 2008.

[27] Y. Li, W. Qiang, S. Lin, and H. Wang, "Particle-in-cell simulation of saturation process of multipactor in parallel-plate transmission lines," in *Proc. IEEE Int. Vac. Electron. Conf. (IVEC)*, Apr. 2015, pp. 1–2.

[28] A. Bossavit, "Whitney forms: A class of finite elements for three-dimensional computations in electromagnetism," *IEE Proc. A, Phys. Sci., Meas. Instrum., Manage. Edu.-Rev.*, vol. 135, no. 8, pp. 493–500, Nov. 1988.

[29] F. L. Teixeira and W. C. Chew, "Lattice electromagnetic theory from a topological viewpoint," *J. Math. Phys.*, vol. 40, no. 1, pp. 169–187, 1999.

[30] F. L. Teixeira, "Lattice Maxwell's equations," *Prog. Electromagn. Res.*, vol. 148, pp. 113–128, Jul. 2014.

[31] W. L. Burke, *Applied Differential Geometry*. Cambridge, U.K: Cambridge Univ. Press, 1985.

[32] H. Flanders, *Differential Forms with Applications to the Physical Sciences*. New York, NY, USA: Dover, 1989.

[33] P. W. Gross and P. R. Kotiuga, *Electromagnetic Theory and Computation: A Topological Approach*. Cambridge, U.K.: Cambridge Univ. Press, 2004.

[34] B. He and F. L. Teixeira, "Differential forms, Galerkin duality, and sparse inverse approximations in finite element solutions of Maxwell equations," *IEEE Trans. Antennas Propag.*, vol. 55, no. 5, pp. 1359–1368, May 2007.

Dong-Yeop Na (S'09) received the B.S. and M.S. degrees in electrical engineering from Ajou University, Suwon, South Korea, in 2012 and 2014, respectively. He is currently pursuing the Ph.D. degree in electrical engineering with The Ohio State University, Columbus, OH, USA.

He is currently a Graduate Research Associate with the ElectroScience Laboratory, The Ohio State University. His current research interests include computational electromagnetics and plasma physics.

Fernando L. Teixeira (F'15) received the Ph.D. degree in electrical engineering from the University of Illinois at Urbana–Champaign, Champaign, IL, USA, in 1999.

From 1999 to 2000, he was a Post-Doctoral Associate with the Massachusetts Institute of Technology, Cambridge, MA, USA. In 2000, he joined The Ohio State University, Columbus, OH, USA, where he is currently a Professor with the Department of Electrical and Computer Engineering and also with the ElectroScience Laboratory. His current research interests include applied electromagnetics and computational physics.

Dr. Teixeira was a recipient of the CAREER Award from the National Science Foundation, the triennial Booker Fellowship from the International Union of Radio Science, and the Outstanding Young Engineer Award from the IEEE Microwave Society (MTT-S). He served as the Chair of the Joint IEEE AP/MTT-S Columbus Chapter. He was an Associate Editor and Guest Editor for IEEE ANTENNAS AND WIRELESS PROPAGATION LETTERS. He serves as an Associate Editor for *IET Microwaves, Antennas, and Propagation*.